

The bidirectional and directional hemispheric reflectance of Apollo 11 and 16 soils: Laboratory and diviner measurements



Emily J. Foote^{a,*}, David A. Paige^a, Michael K. Shepard^b, Jeffrey R. Johnson^c, Stuart Biggar^d

^a University of California Los Angeles, 595 Charles Young Drive East, Box 951567, Los Angeles, CA 90095-1567, United States

^b Bloomsburg University, 400 E. Second St., Bloomsburg, PA 17815, United States

^c Johns Hopkins University Applied Physics Laboratory, 11101 Johns Hopkins Road, 200-W230, Laurel, MD 20723-6005, United States

^d College of Optical Sciences, University of Arizona, 1630 E. University Blvd., P.O. Box 210094, Tucson, AZ 85721-0094, United States

ARTICLE INFO

Keywords:

Moon
Radiative transfer
Photometry
Surface

ABSTRACT

We have acquired a comprehensive laboratory bidirectional measurements of Apollo 11 and Apollo 16 lunar soil samples and have successfully fit photometric models to the laboratory data and have determined the solar spectrum averaged hemispheric reflectance as a function of incidence angle. The Apollo 11 (sample 10,084) and 16 (sample 68,810) soil samples are two representative end member samples from the Moon, dark lunar maria and bright lunar highlands. We used our solar spectrum averaged albedos in a thermal model and compared our model-calculated normal bolometric infrared emission curves with those measured by the LRO Diviner Lunar Radiometer Experiment. We found excellent agreement at the Apollo 11 site, but at the Apollo 16 site, we found that the albedos we measured in the laboratory were 33% brighter than those required to fit the Diviner infrared data. We attribute this difference at Apollo 16 to increased compaction and decreased maturity of the laboratory sample relative to the natural lunar surface, and to local variability in surface albedos at the Apollo 16 field area that are below the spatial resolution of Diviner.

1. Introduction

The bolometric hemispheric reflectance is the total reflected energy from a surface for a given solar incidence angle (Hapke, 1993). Determining the bolometric hemispheric reflectance of the Lunar surface is important because of the key role it plays in the surface energy balance. It determines the radiative equilibrium temperature of the surface (Hapke, 1993), and it is thus a key input for lunar thermal models. The bolometric hemispheric reflectance cannot be fully measured from orbit, but it can be measured in the laboratory by integrating spectrophotometers or by goniometers. The first measurements of the hemispheric reflectance of lunar samples were made by Birkeback and Cremers (1970) who used an integrating spectrophotometer to measure the directional spectral and total reflectance of newly acquired soil samples from Apollo 11. Their results have been incorporated into subsequent thermal models of the lunar surface (Keim 1984; Vasavada et al., 1999, 2012; Hayne et al., 2017). This study presents the results of a new set of laboratory bi-directional reflectance measurements of two Apollo regolith samples which are interpreted in terms of the bolometric

hemispheric reflectance.

One of the main motivations for this work is to obtain full Bidirectional Reflectance Distribution Functions (BRDF's) for representative lunar maria and highlands samples. The BRDF allows calculation of reflectance at any combination of photometric angles as well as the integrated hemispheric reflectance. In this study, we measured the full bidirectional reflectance distribution functions of two lunar soil samples from the Apollo 11 and 16 missions. We then fit two BRDF models, one theoretical and one empirical, to the laboratory data and computed the bolometric hemispheric reflectance. We next used our derived bolometric hemispheric reflectances in conjunction with a one-dimensional thermal model to calculate the bolometric infrared emission at the Apollo 11 and Apollo 16 landing sites, and compared these results with diurnal bolometric thermal emission measurements made by the Lunar Reconnaissance Orbiter Diviner Lunar Radiometer Experiment, DIVINER (Paige et al., 2010a).

* Corresponding author.

E-mail addresses: efoote@ucla.edu (E.J. Foote), dap@moon.ucla.edu (D.A. Paige), mshepard@bloomu.edu (M.K. Shepard), Jeffrey.R.Johnson@jhuapl.edu (J.R. Johnson), biggar@optics.arizona.edu (S. Biggar).

<https://doi.org/10.1016/j.icarus.2019.113456>

Received 1 March 2018; Received in revised form 2 August 2019; Accepted 27 September 2019

Available online 30 September 2019

0019-1035/© 2019 Published by Elsevier Inc.

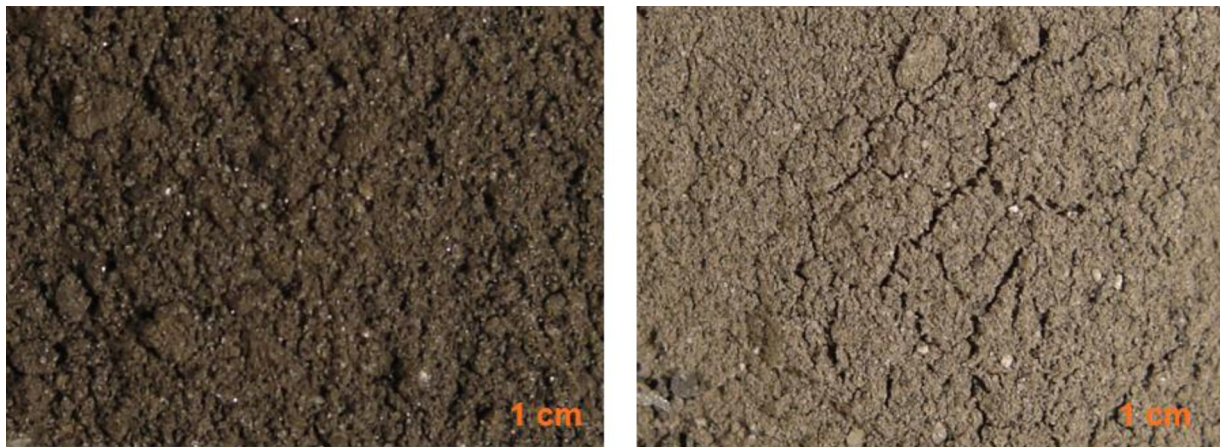


Fig. 1. Close up images of the Apollo 11 and 16 lunar soil samples. The width of each closeup sample image is 1 cm.

Table 1

Descriptions of Apollo samples used in this study from The Handbook of Lunar Soils (Handbook of Lunar Soils, 1983) We measured the bulk density of Highland sample (68,810) and Mare sample (10,084) in our lab (see text). Note: average grain size.

Sample Name	Grain Size	Maturity	Petrography	Color	Major Elements	Bulk Density
Apollo 10,084	< 1 mm	mature (I/Fe –74.0 and agglutinates)	24% mare basalt, 52% agglutinates, 4.2% mafic mineral fragments, 4.8% glass fragments	medium gray	41% SiO ₂ , 12.8% Al ₂ O ₃ , 7.3% TiO ₂ , 16.2% FeO	1.512878151
Apollo 68,810 (68,820)	112 μm	mature (I/Fe –84.0 and agglutinates)	15% plagioclase, 52% agglutinates, 22% breccias	olive gray	44.5% SiO ₂ , 26.2% Al ₂ O ₃ , 0.5% TiO ₂ , 5% FeO, 6.13% MgO, 15.3% CaO	1.26572479
Apollo 61,141	78 μm	submature (I/FeO - 56.0 and agglutinates)	15% medium grade breccias, 14.7% feldspar, 37.0% agglutinates, 13.6% low-grade colorless breccias	medium brownish gray	45.2% SiO ₂ , 26.4% Al ₂ O ₃ , 0.58% TiO ₂ , 5.29% FeO, 6.10% MgO, 15.32% CaO	1.006588235

Notes: Descriptions for Apollo 68,810 were substituted with the adjacent Apollo 68,820 sample information, because Apollo 68,810 has not been characterized. It was given to us as a test sample. Dick Morris (JSC) made the maturity measurement of our Apollo 68,810 sample.

2. Materials and methods

2.1. Samples

The Curation and Analysis Team for Extraterrestrial Materials (CAPTEM) at NASA provided two representative lunar soil samples: a typical low albedo mare sample (10,084, Apollo 11), and a high albedo lunar highlands soil (68,810 & 61,141, Apollo 16) (Fig. 1). Descriptions of each of our samples can be found in Table 1, which includes petrography, grain size, maturity and major elements. For our purposes,

maturity is defined as the degree of surface exposure to micrometeorites and solar wind which particular soil has experienced. The specific information was derived from the Lunar Soil Handbook (Handbook of Lunar Soils, 1983) Table 1 also shows our measurements of the bulk density of our two lunar soil samples, which was accomplished by measuring the weights of the samples in a 2.5 ml volume.

For this study, CAPTEM generously loaned us 28.578 g of the Apollo 11 lunar soil sample 10,084 and 52.000 g of the Apollo 16 lunar soil sample 68,810 and 20 g of lunar soil sample 61,141. The Apollo 11 sample is a basaltic regolith that has a substantial non-mare component.

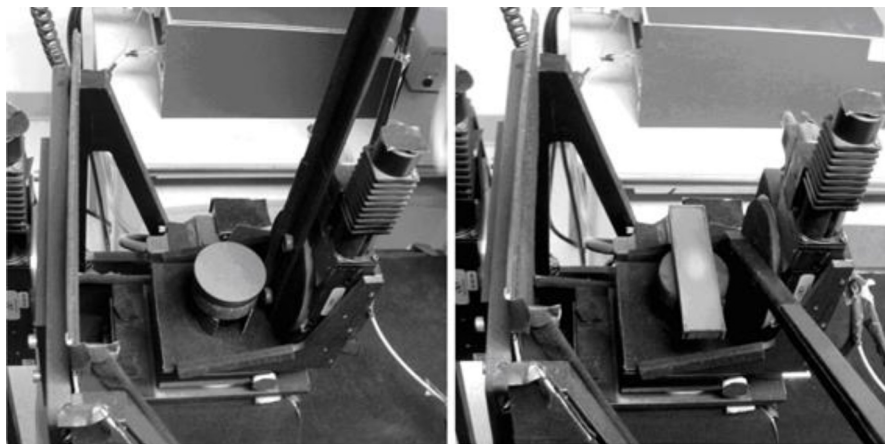


Fig. 2. The BUG experimental setup for measuring Bidirectional Reflectance Distribution Functions (BRDF). (left) The standard BUG setup uses a sample cup with a diameter of 6 cm and a depth of 0.5 cm. (right) The nonstandard BUG setup for measurements along and perpendicular to the principal plane axis using a 12 cm × 2.5 cm × 0.5 cm dish, which enabled acquisition of data at high incidence angles ($i > 60^\circ$).

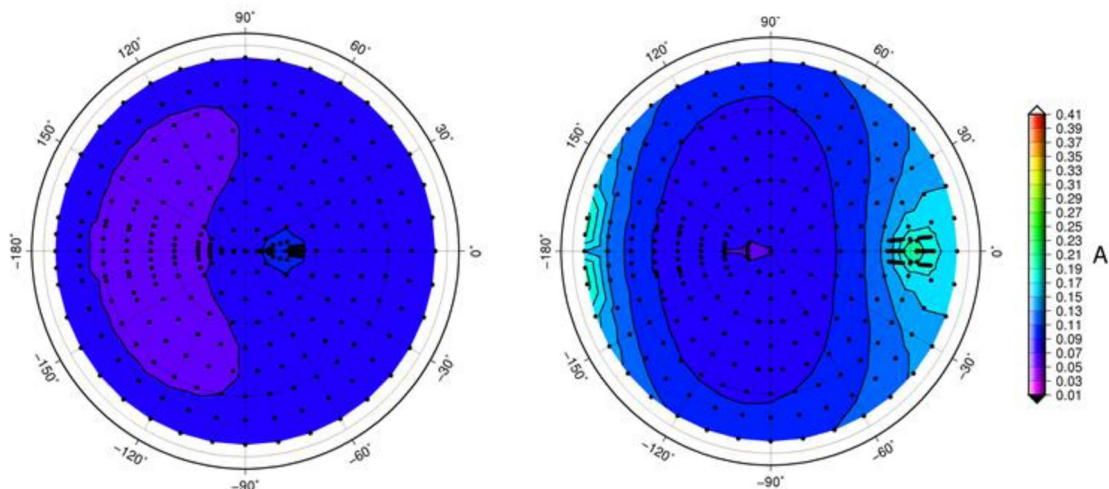
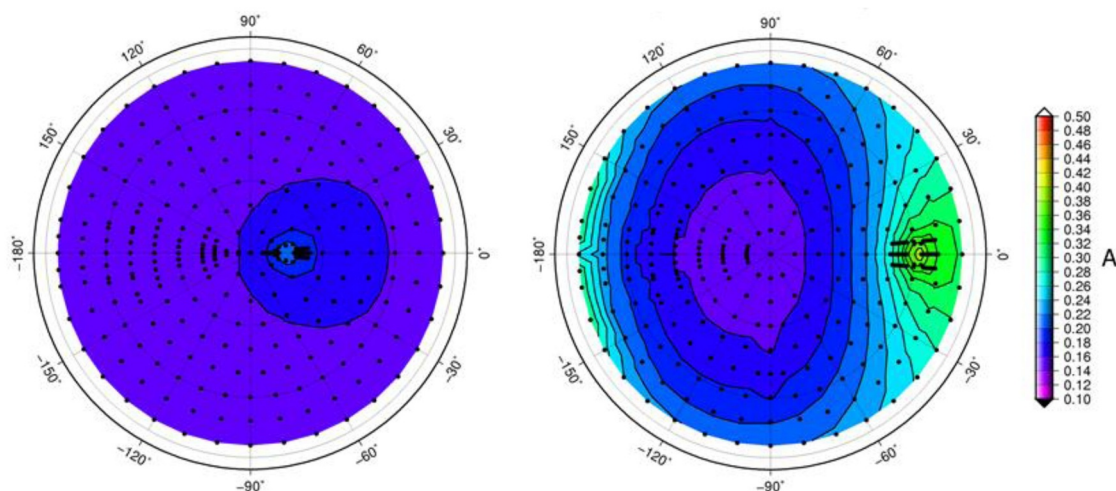
Apollo 11, $i=15^\circ$ and $i=60^\circ$ Apollo 16, $i=15^\circ$ and $i=60^\circ$ 

Fig. 3. Polar contour plots of measured Lambert Albedo (A) where e is radial coordinate and ψ is the azimuthal coordinate (see figure 8.1 in Hapke, 1993 for graphical depiction of the angle). Dots denote BUG angle sets. Shown are measurements for $i = 15^\circ$ and $i = 60^\circ$ for both Apollo 11 (top 2) and Apollo 16 (bottom 2). The illumination source is along the positive x axis. The radial coordinate is emission angle (to 90°) and the azimuthal coordinate is azimuth angle, where 0° azimuth defines the plane of incidence. The principal plane is oriented along the x axis.

The composition is 66% crystalline mare basalt, 20% feldspathic particles from the highlands, 8% KREEP-bearing, impact-melt breccias, 5% orange volcanic glass and 1% meteoritic material (Korotev and Gillis, 2001). Unfortunately, the Apollo 16 sample has not yet been characterized in detail. However, other Apollo 16 soil samples (e.g. 68,820) that have been characterized are primarily composed of impact breccias and anorthositic rocks (Handbook of Lunar Soils, 1983). Fig. 1 is a close up image of our two lunar soil samples.

The samples used in our study are not pristine. We cannot say for certain they weren't contaminated from terrestrial exposure. Previous research looked at the effects of hydration and found the absorption feature of water near $3 \mu\text{m}$ in pristine lunar soil samples (Izawa et al., 2014). Milliken and Mustard (2007) also made spectral reflectance measurements on fine particle samples and studied how the absorption of water changes the reflectance. Spectral variations near $3 \mu\text{m}$ will not have an impact on our analyses because the magnitude of the solar flux is very small in this spectral region. Also, Birkebak et al. (1970)

measured the directional reflectance of Apollo Lunar soil, sample 10, 084, in a vacuum and at standard atmospheric pressure which yielded no spectral absorption features from $0.5 \mu\text{m}$ to $2.0 \mu\text{m}$.

2.2. BUG apparatus

We used the Bloomsburg University Goniometer (BUG) (Shepard et al., 2002) to make the Bidirectional Reflectance Distribution Function (BRDF) measurements on the Apollo samples. The BUG instrument consists of a filtered, chopped and collimated light source and a solid-state detector. The source and detector move along three independent axes. The source is a 100 W quartz halogen bulb and is attached to an arm that moves $0-65^\circ$ degrees in incidence (i) and $0-180^\circ$ degrees in azimuth, 60 cm away from the sample. The detector is attached to an arm that moves $0-80^\circ$ in emission (e) angle, 80 cm away from the sample. Fig. 2 shows the BUG experimental setup which was optimized for obtaining reflectance measurements at high incidence and emission

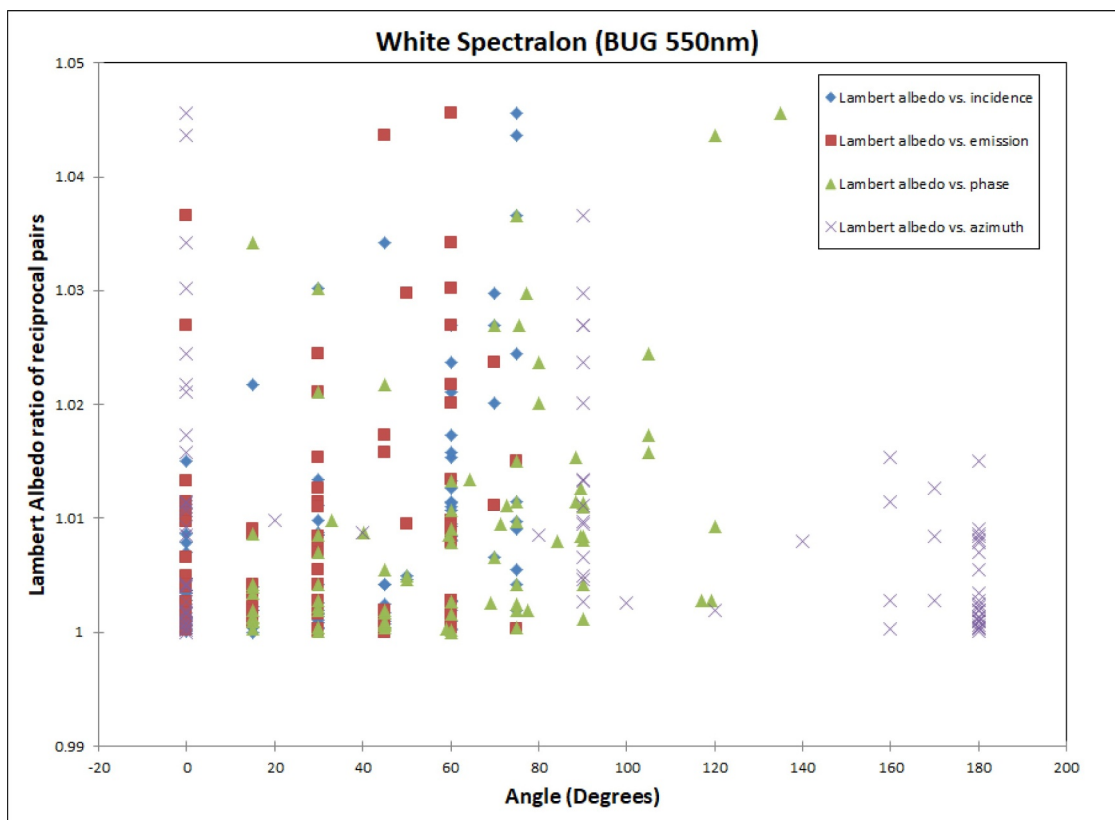


Fig. 4. Reciprocity check of the spectralon measurements made on BUG. The majority of the points fall along 1.00. The average value of the 47 reciprocal pairs is 1.0092345.

angles. We prepared the sample by carefully pouring it into a small dish and leveling the surface with a straight edge. Fig. 2 also shows the prepared sample on the goniometer in between measurements.

2.3. Data acquisition, calibration and verification

The BUG instrument is calibrated before and after each run. This calibration procedure included measuring the raw intensity in voltage of a Spectralon reference target, certified to NIST standards, at an incidence angle, $i = 0^\circ$ and emission angle, $e = 5^\circ$ (Shepard and Helfenstein, 2007, 2011).

We collected two different types of BUG reflectance datasets. The standard set of BUG BRDF measurements includes a set of incidence angles ($0^\circ < i < 60^\circ$), emission angles ($0^\circ < e < 80^\circ$), and phase angles ($3^\circ < g < 140^\circ$), which provided us with 680 measurements per wavelength (Shepard and Helfenstein 2007, 2011, and Johnson et al., 2013) (see Fig. 3). We also obtained separate BUG datasets at high-incident angles. These measurements were acquired along and perpendicular to the principal plane axis and include incidence angles $0^\circ < i < 75^\circ$ and phase angles $3^\circ < g < 155^\circ$, which gave us an additional 89 points per wavelength (for a grand total of 769 angle combinations). We used 4 narrow-band spectral filters to obtain the following data sets: 450, 550, 750, and 950 nm (Johnson et al., 2009).

The BUG measures the radiance factor r_f , which is the ratio between the measured intensity to that of a normally illuminated perfectly reflecting diffuse (Lambert) surface. Since r_f varies with illumination geometry, the bidirectional reflectance is most easily visualized in terms of the Lambert albedo, which is the ratio to the measured reflectance relative to that of a Lambert surface measured under the same illumination condition (Hapke, 1993; Shepard, 2017). For this work, we define Lambert albedo as:

$$A_L = r_f / \mu_0 \quad (1)$$

Where μ_0 is the cosine of the incidence angle.

We verified our BUG BRDF measurements in three ways. First, we checked reciprocity for measurements of a white Spectralon target for several sets of angles (Fig. 4). We examined the ratio of Lambert albedos of 47 reciprocal pairs as a function of azimuth angle, phase angle, emission angle and incidence angle. As illustrated in the plot, the BUG measurements obey the Helmholtz reciprocity principle also known as Principle of Reciprocity (Minnaert, 1941 and Shepard, 2017) to a high degree, as the average Lambert albedo ratio is 1.0092345. Also, noticeable is how the majority (approximately 67%) of the values fall along the 1.00 line.

For our second verification, we did a cross calibration check between the BUG goniometer at 550 nm and the Blacklab goniometer at the University of Arizona Optical Sciences Lab at 554 nm (Biggar et al., 1988; 2003). The Blacklab goniometer was used previously to measure the bidirectional reflectance of the Diviner flight solar calibration target (Paige et al., 2010a). The Blacklab measurements of the two spectralon targets were calibrated relative to a prepared Algonon targets whose bidirectional reflectance for normal illumination, and whose integrated hemispheric reflectance was directly traceable to NIST standards. Comparing Blacklab to BUG revealed that the calibration procedures previously employed by BUG resulted in absolute reflectances that were systematically lower than Blacklab by a factor of 0.955. Fig. 5 shows corrected BUG vs Blacklab Spectralon reflectances from Shepard and Helfenstein (2011). To make our BUG lunar sample measurements consistent with Blacklab, we applied a correction factor of 1.047 to all our BUG data.

For our third verification, we measured the same Apollo 11 lunar soil

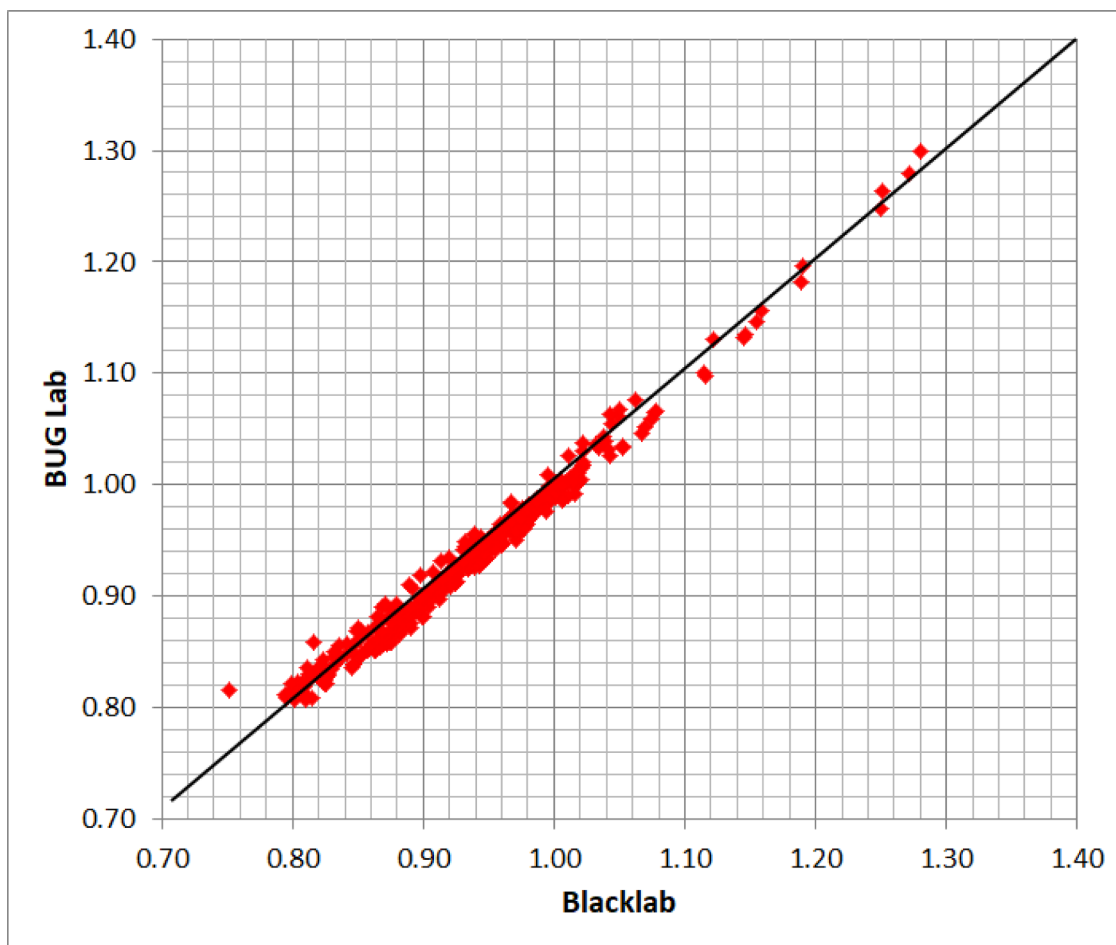


Fig. 5. Comparison of Lambert Albedo spectralon measurements made on BUG and Blacklab from [Shepard and Helfenstein \(2011\)](#).

sample with Blacklab at 455, 554, 699 and 949 nm and with BUG at 450, 550, and 950 nm for a restricted set of 25 photometric angles ($60^\circ < i < 75^\circ$), ($60^\circ < e < 80^\circ$), and ($51^\circ < g < 94^\circ$) and found that the ratios of Blacklab to corrected BUG reflectances were 1.0028 at 455/450 nm, 1.0066 at 554/550 nm, 0.963 at 699/750 nm, and 1.046 at 949/950 nm.

3. BUG dataset

The BUG reflectance data are presented in terms of the Lambert Albedo. A Lambert surface has a constant Lambert albedo at all illumination and viewing geometries, and therefore represents the simplest surface BRDF model. Another useful surface BRDF model is the Lommel-Seeliger (L-S) model, which can be derived from radiative transfer theory under the assumption of an infinitely deep medium consisting of isotropically single scattering particles (i.e. no multiple scattering). The L-S albedo is related to the Lambert albedo through the following relation:

$$A_{L-S} = (\mu_0 + \mu)A_L \quad (2)$$

Where $\mu = \cos e$ ([Shepard, 2017](#)).

[Figs. 3 and 6-9](#) show representative plots of the measured BUG Lambert albedos for the Apollo 11 and 16 samples. The results are presented in 3 different ways: contour plots using all the data; only data along the principal plane; and, only data perpendicular to the principal plane. The lunar BRDF's exhibit strong peaks in reflectance at low phase angles, which is a manifestation of the well-known lunar opposition effect ([Hapke, 1993; Shepard, 2017](#)). [Fig. 10](#) shows L-S albedos for the

BUG Apollo 11 results in the principal plane. The general consistency of the L-S albedo peaks at $g = 0$ suggests that the single scattering phase functions for soil particles are the dominant factor in determining the BRDF for the Apollo 11 soil sample. This is expected behavior for dark materials consisting of particles with low single scattering albedo, which reduces the effects of multiple scattering. ([Hapke, 1993; Goguen, et al., 2010](#))

4. BRDF models and results

One of the main motivations for this work is to obtain a full BRDF and find a photometric model that fits the Apollo 11 and 16 BUG datasets. The model fits enable the calculation of BRDF's at any combination of photometric angles, and to determine the hemispheric bolometric reflectance. We chose two models to fit the BUG BRDF data - [Hapke's 1993 BRDF model](#) and a simplified empirical BRDF model that we developed specifically for this study.

4.1. Hapke model

We used Hapke's equation (12.55) ([Hapke, 1993](#)) for the bidirectional-reflectance distribution function (BRDF) of a rough surface. Hapke's models are based on a combination of radiative transfer modeling and empirical parameterizations. This version of Hapke's model was chosen because of its widespread use in the field, and because it was the least complex version that includes enough free parameters to obtain accurate fits. [Hapke's 1993 BRDF equation](#) (Equation 12.55) can

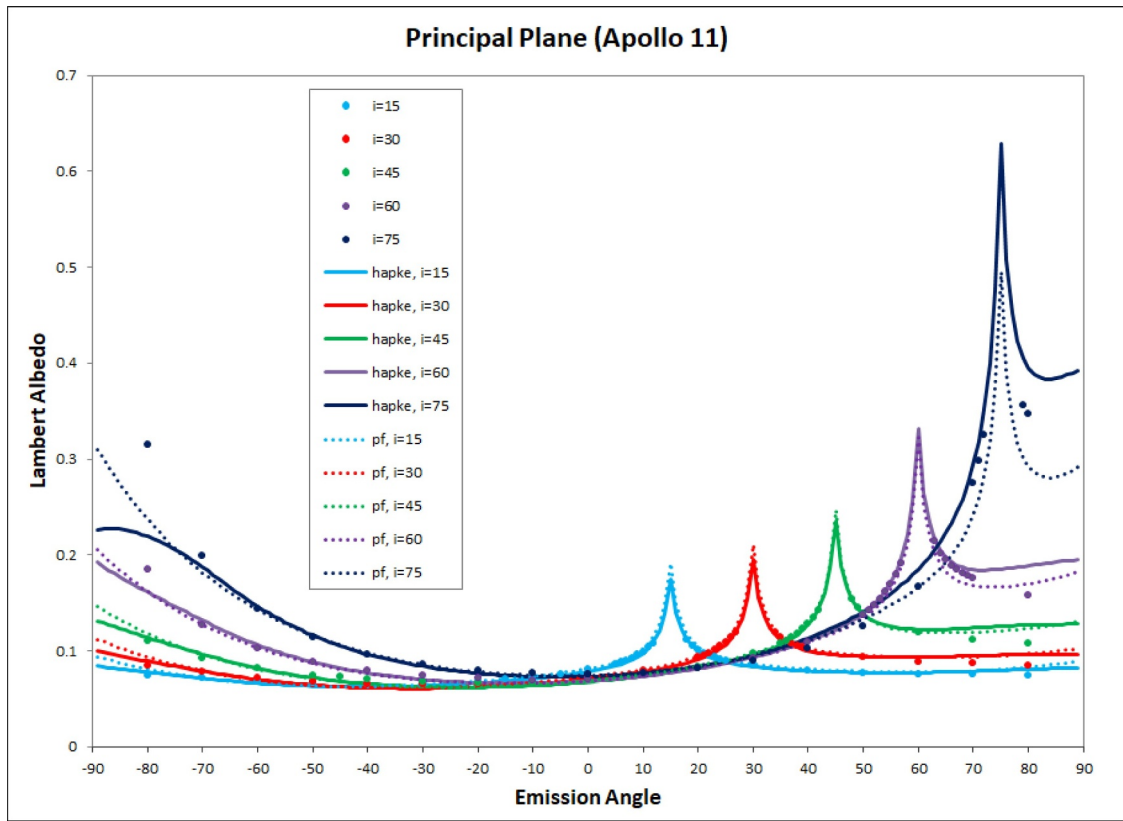


Fig. 6. Lambert Albedo plots along the principal plane of the Apollo 11 BUG data (dots), Hapke (solid lines) and Simplified (dashed lines) functions using the best fit parameter values shown in Table 2 for the 750 nm wavelength datasets. Each color represents a different fixed incidence angle. Both functions fit the BUG data very well at low incidence angles and fit fairly well at the higher incidence angles.

be expressed in terms of the Lambert Albedo:

$$A_L = \frac{w}{4\mu_0} \frac{\mu_{0e}}{\mu_{0e} + \mu_e} \{ [(1 + B(g))p(g) + H(\mu_{0e})H(\mu_e) - 1] S(i, e, g) \} \quad (3)$$

where w is the single scattering albedo, μ_{0e} and μ_e are the computed effective cosines of the incidence and emission angles accounting for surface roughness, $B(g)$ is a backscattering function for the opposition

effect, $p(g)$ is the single scattering phase function, H are the Chandrasekhar (1960) “H” functions that account for multiple scattering, for which we employed Hapke’s simplified equation 8.50, and $S(i, e, g)$ is a shadowing/visibility function, equation 12.50 (Hapke, 1993).

Following Johnson et al. (Johnson et al., 2006), we use:

$$B(g) = B_0 / \left(1 + \frac{\tan(g/2)}{h} \right) \quad (4)$$

Table 2

Best fit parameters for the Apollo 11 (top) and Apollo 16 (bottom) 450, 550, 750 and 950 nm BUG Data using the Hapke BRDF and a simplified BRDF.

Apollo 11		Common Parameters				Simplified Parameters		Hapke Parameters		
Dataset	BRDF Model	b	c	h	b0	x	y	w	θ	χ^2_v
450	Simplified All BUG	0.2615385	0.4025641	0.034310345	1.255172	0.046764705	0.4279412	n/a	n/a	0.3402105
	Hapke All	0.3	0.4051724	0.010833333	2.485294	n/a	n/a	0.2514706	10.75	0.4156695
550	Simplified All BUG	0.2615385	0.3935897	0.029137932	1.255172	0.057941176	0.4764706	n/a	n/a	0.32275875
	Hapke All	0.2916667	0.4051724	0.010833333	2.485294	n/a	n/a	0.2882353	10.5	0.39432425
750	Simplified All BUG	0.2538462	0.4025641	0.01362069	1.77931	0.074705884	0.4926471	n/a	n/a	0.259549
	Hapke All	0.2916667	0.4051724	0.009375	2.632353	n/a	n/a	0.3470588	10.25	0.339313
950	Simplified All BUG	0.2538462	0.3846154	0.011896552	1.975862	0.080294117	0.5088235	n/a	n/a	0.3369905
	Hapke All	0.2916667	0.3965517	0.007916667	2.926471	n/a	n/a	0.3617647	9.75	0.413209
Apollo 16		Common Parameters				Simplified Parameters		Hapke Parameters		
Dataset	BRDF Model	b	c	h	b0	x	y	w	θ	χ^2_v
450	Simplified All BUG	0.2153846	0.4833333	0.051551722	1.124138	0.091470592	0.4764706	n/a	n/a	0.212062
	Hapke All	0.2770833	0.5051724	0.016249999	1.897059	n/a	n/a	0.4220588	10.25	0.250006
550	Simplified All BUG	0.2153846	0.4833333	0.04465517	0.9931034	0.1138235	0.5088235	n/a	n/a	0.2005311
	Hapke All	0.2770833	0.4948276	0.010625	2.411765	n/a	n/a	0.4838235	10.25	0.2386586
750	Simplified All BUG	0.2076923	0.474359	0.037758619	0.9275862	0.1529412	0.6058824	n/a	n/a	0.20115355
	Hapke All	0.2770833	0.4741379	0.010625	2.264706	n/a	n/a	0.5661764	10.5	0.223534075
950	Simplified All BUG	0.2153846	0.4564103	0.030862067	0.862069	0.1808823	0.7029412	n/a	n/a	0.199690175
	Hapke All	0.2979167	0.4431034	0.006875	2.632353	n/a	n/a	0.6073529	11	0.223350275

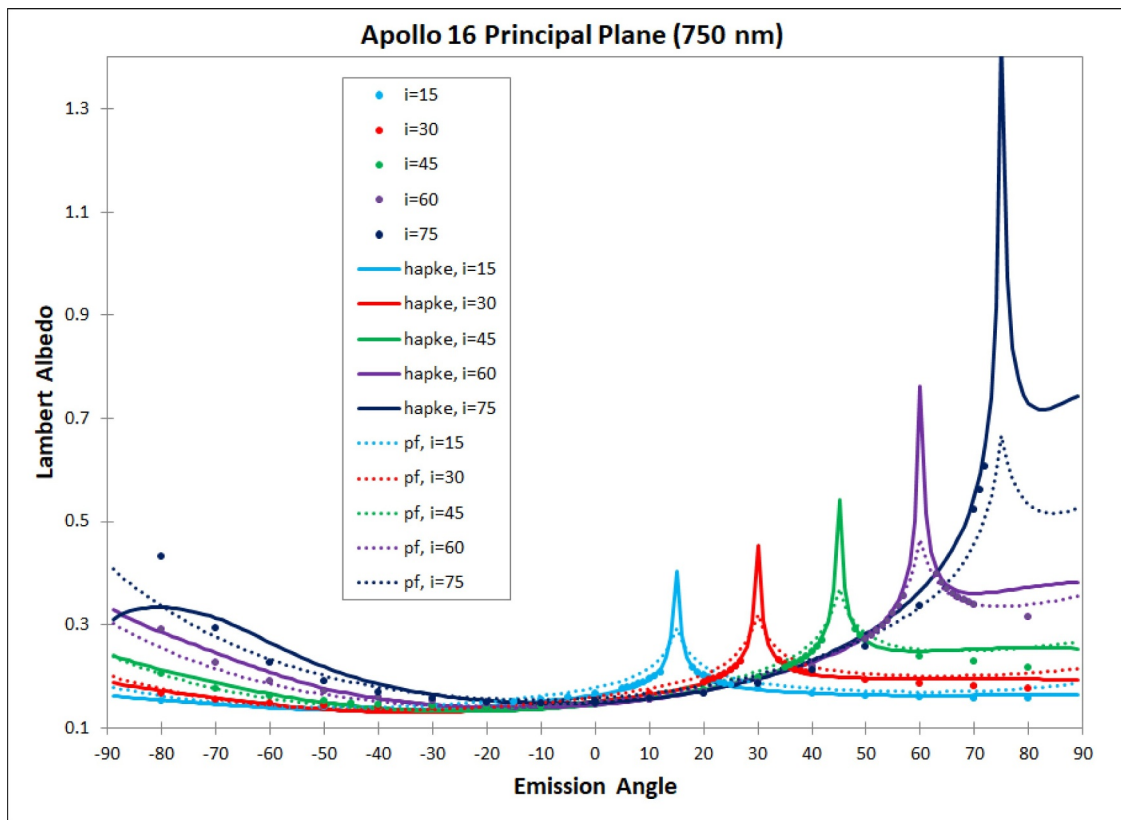


Fig. 7. Lambert Albedo plots along the principal plane of the Apollo 68810 BUG data (dots lines), Hapke (solid lines) and Simplified (dashed lines) functions using the best fit parameter values shown in Table 2 for the 750 nm wavelength datasets. Each color represents a different fixed incidence angle. Both functions fit the BUG data very well at low incidence angles and fit fairly well at the higher incidence angles.

and

$$p(g) = \frac{c(1-b^2)}{(1-2bcos(g)+b^2)^{3/2}} + \frac{(1-c)(1-b^2)}{(1+2bcos(g)+b^2)^{3/2}} \quad (5)$$

Where B_0 is the amplitude of the shadow hiding opposition surge and h is the angular width of the shadow hiding opposition surge. $p(g)$ is approximated as the 2-term Henyey-Greenstein function. Where c represents the backward scattering fraction and b is the asymmetry parameter.

4.2. Simplified empirical model

We have developed a simplified empirical function that yields BRDF behavior that is similar to Hapke's, but is significantly less computationally intensive. The Simplified Empirical BRDF Model is:

$$A_L = \frac{2X}{(\mu_0 + \mu + Y)} \frac{1}{\mu_0} (1 + B(g))p(g) \quad (6)$$

where μ_0 is the cosine of the actual incidence angle and μ is the cosine of the actual emission angle, and X and Y are empirical constants. X is a multiplicative factor that determines the overall reflectance, and Y prevents the function from blowing up at high phase angles when μ_0 and μ are small. $B(g)$ is the same as Eq. (4) above. Like the Hapke models, the simplified empirical model satisfies the Helmholtz reciprocity principle in that exchanging μ_0 for μ results in an equation is mathematically equivalent (Minnaert, 1941), but it ignores multiple scattering and shadow hiding Hapke terms in his original equation.

4.3. BRDF results

We successfully fit the BUG data with the two BRDF models described above using a fitting procedure in which we selected a range of parameter values and time step for each parameter and tried every combination until the sum of squares was minimized. As shown in Table 2, we obtained best fit reduced chi-squared χ^2_v values between 0.2 and 0.3, which indicates that the data are well fit by both models. The χ^2_v values for the Apollo 16 data are systematically lower than those for Apollo 11, due to the fact that we likely overestimated the uncertainty in the BUG data for the brighter Apollo 16 sample. We assumed that each of the BUG measurements had the same uncertainty value and the absolute systematic error was 4% ($\sigma=0.04$), based on Johnson et al., 2013. Although, according to Sheppard and Helfenstein, 2007 the uncertainties in the high emission BUG data ($i=60^\circ$, $e=80^\circ$) tend to be 5–10% larger.

Recognizing that derived parameters from Hapke's model are non unique (Shepard and Helfenstein, 2007), we employed it because of its wide use in the field, and because it has enough free parameters to obtain accurate fits. The average single scattering albedos (w) for the Mare Apollo 10,084 sample is 0.32 and for the highlands Apollo 68,810 and 61,141 samples are 0.54 and 0.58, respectively. All of the values for our Hapke fits are shown in Table 2. Johnson et al. (2013) used a similar Hapke model to fit the same BUG measurements and computed Hapke values that are similar to ours. Both Apollo samples and Hapke fits to the BUG data show decreasing c values (greater forward scattering) and increased b values with wavelength. (Johnson et al., 2013).

Examples of BRDF model Lambert albedos are shown in Figs. 11 and 12. The principal plane results are shown in Figs. 6, 7 and 10 and the off

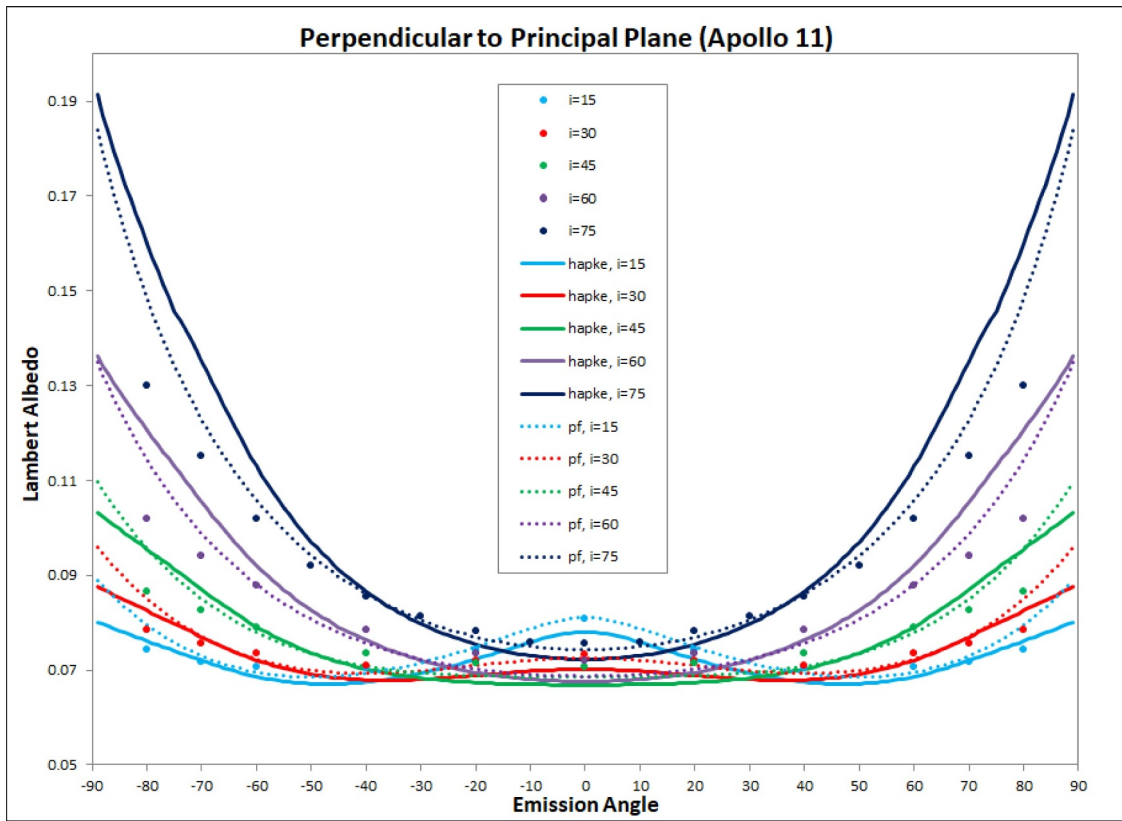


Fig. 8. Perpendicular to Principal plane plots of the Apollo 11 BUG data (dots lines), Hapke (solid lines) and Simplified (dashed lines) functions using the best fit parameter values shown in Table 2 for the 750 nm wavelength datasets. Each color represents a different fixed incidence angle. Both functions fit the BUG data very well at low incidence angles, but overestimate at higher incidence angles, $i > 30^\circ$

principal plane results are shown in Figs. 8 and 9. The results show that both approaches can satisfactorily fit the BUG data. This is not completely unexpected, given the similarities between the functions and their input parameters, and the fact that the BRDF for dark lunar soil is likely to be dominated by the single scattering phase functions of the individual soil particles. However, both BRDF models tend to somewhat underestimate the BUG data when incidence and emission angles are both high, which is due to the fact that most of the fitted data were acquired at lower incidence angles.

5. Solar spectrum averaged hemispheric albedo results

The heat balance of the lunar surface is controlled by the solar spectrum averaged hemispheric albedo, which is sometimes referred to as the bolometric albedo, or the directional hemispheric reflectance. We determine the directional hemispheric albedo, A_h , as a function of incidence angle at each measured BUG wavelength, using Hapke's Eq. 10.10:

$$A_h(i) = \pi \int_{2\pi} A_L(i, e, g) \mu d\Omega_e \quad (7)$$

where $d\Omega_e = \sin e \, ded\psi$ and ψ is the azimuth angle. To calculate solar spectrum average directional hemispheric albedoes, we calculated appropriate spectral boundaries and solar spectrum weighting factors for each BUG filter and linearly extrapolated the directional hemispheric albedos for wavelengths shorter than 450 nm and for wavelengths longer than 950 nm based on published measurements of lunar soil spectral reflectance in these wavelength ranges (Ohtake et al., 2013; Izawa et al., 2014). Solar spectrum integration parameters shown in Table 3 are based on the ASTM E490-00a (ASTM International, 2014)

solar spectrum data. The best fit Hapke values that we used to calculate the bolometric reflectance curves are shown in Table 4.

Fig. 13 shows the solar spectrum averaged hemispheric albedos for the Apollo 11 and 16 BUG measurements as a function of incidence angle. We fit 2nd-order quadratic functions to the standard mare soil sample (Apollo sample 10,084) and to the standard highlands sample (Apollo sample 61,141) for $A_L(i)$ where i is in degrees. The second order polynomial fit for the mare Apollo sample 10,084 is:

$$A_h(i) = 9.4032 * 10^{-6} i^2 - 1.8345 * 10^{-4} i + 0.068061 \quad (8)$$

The second order polynomial fit for the lightest highlands Apollo sample (Apollo 16) is:

$$A_h(i) = 1.3299 * 10^{-5} i^2 - 1.0248 * 10^{-4} i + 0.14382 \quad (9)$$

Also included on the same plot are Kheim's (1984) model and Vasavada's (1999 and 2012) models for the same quantity. The functional dependence of albedo on solar incidence angle previously published by Kheim and Vasavada (Kheim, 1984) and (Vasavada et al., 1999 & 2012) is:

$$A_h(i) = A_0 + a(i/45)^3 + b(i/90)^8 \quad (10)$$

The parameter values that Kheim used are constrained for the entire lunar surface as $A_0=0.12$, $a=0.03$, $b=0.14$. Vasavada et al. (2012) splits the lunar surface into two bolometric hemispherical reflectance functions; mare: $A_0=0.07$, $a=0.045$, $b=0.14$ and highlands: $A_0=0.16$, $a=0.045$, $b=0.14$.

As shown in Fig. 13, the hemispheric reflectance functions derived from our laboratory measurements of the Apollo soil samples display relatively flat curves with increasing incidence angles, while the functions employed by Kheim and Vasavada dramatically increase beyond

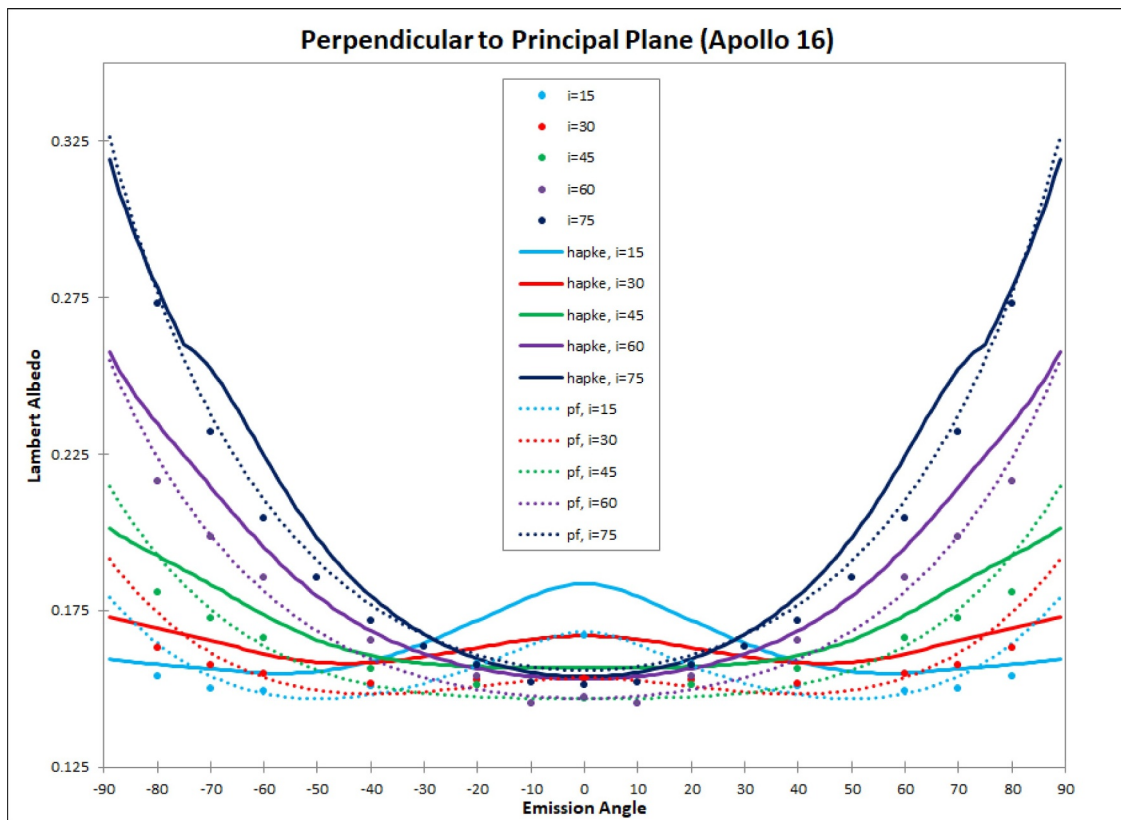


Fig. 9. Perpendicular to Principal plane plots of the Apollo 16 BUG data (dots lines), Hapke (solid lines) and Simplified (dashed lines) functions using the best fit parameter values shown in Table 2 for the 750 nm wavelength datasets. Each color represents a different fixed incidence angle. Both functions fit the BUG data very well at low incidence angles and fit fairly well at the higher incidence angles.

50° incidence angle. For example, the absolute difference between their models and our measurements of both Apollo samples at 60° is 0.1. Kheim's ($A_0=0.12$) and Vasavada's ($A_0=0.07$ for the mare regions and $A_0=0.16$ for highlands) models have higher initial albedo values than what we measured at normal illumination conditions ($A_0=0.0644$ for the mare Apollo 11 samples and $A_0=0.14$ for highlands Apollo 16 sample). The impacts of these differences on thermal model results are described in later sections.

6. Diviner bolometric brightness temperature measurements

We determined normal bolometric brightness temperatures from the Apollo 11 and Apollo 16 sample sites using data acquired by Diviner. The bolometric brightness temperature provides a means of characterizing wavelength-integrated thermal emission measurements in terms of an equivalent blackbody emitter (Paige et al., 2010b). Since lunar surface temperatures are close to being in radiative equilibrium during the daytime, measured bolometric brightness temperatures may provide a useful check on models for the hemispheric albedo.

Precise locations for the Apollo sampling stations have been determined by the LRO LROC team (<http://www.lroc.asu.edu/>), and we found the coordinates of our sampling sites using the online Quickmap tool in conjunction with Apollo-era maps provided in the Handbook of Lunar Soils (1983). Our coordinates for the Apollo 11 sample are (0.67370546°N, 23.4724216°E) and for our Apollo 16 sample are (-9.0687°N, 15.4755°E). We retrieved all Diviner data obtained between July 2009 and August 2016 in Channels 3–9 with $0^\circ < e < 5^\circ$ within 30 km latitude/longitude boxes centered at these locations and binned them at a resolution of 0.25 h in local time. The chosen sizes of the

latitude/longitude boxes was the result of a tradeoff between the desire for high spatial resolution and the desire for high local time resolution and coverage. We then computed bolometric brightness temperatures as described by Paige et al. (2010b). We also computed a small correction to the daytime bolometric brightness temperatures (obtained between 6 and 18 h local time) to account for the ~7% annual variation in the solar flux due to the eccentricity of the Earth's orbit around the Sun by multiplying the bolometric thermal emission by the square of the Sun-Earth distance in AU. The seasonal effects due to the small (1.54°) obliquity of the Moon are negligible at these latitudes so no correction was applied for this. The relationship between the corrected bolometric brightness temperatures, T_{BolC} and the measured T_{bol} values is:

$$\sigma T_{BolC}^4 = \sigma T_{bol}^4 R_{\oplus}^2 \quad (11)$$

Where R_{\oplus} is the Sun-Earth distance in AU. The resulting T_{BolC} values for Apollo 11 and Apollo 16 $R_{\oplus} < 1$ (close) and $R_{\oplus} > 1$ (far) are shown in Figs. 14 and 15.

7. Thermal model results

We employed a thermal model that is equivalent to the model described by Hayne et al. (2017) to calculate bolometric brightness temperatures to compare with the Diviner data. The model surface heat balance equation can be written as:

$$K \frac{\partial T}{\partial z} + (1 - A_h(i))S = \epsilon \sigma T^4 \quad (12)$$

where K is the thermal conductivity, $\frac{\partial T}{\partial z}$ is the vertical temperature gradient at the surface, S is the incident solar flux, ϵ is the

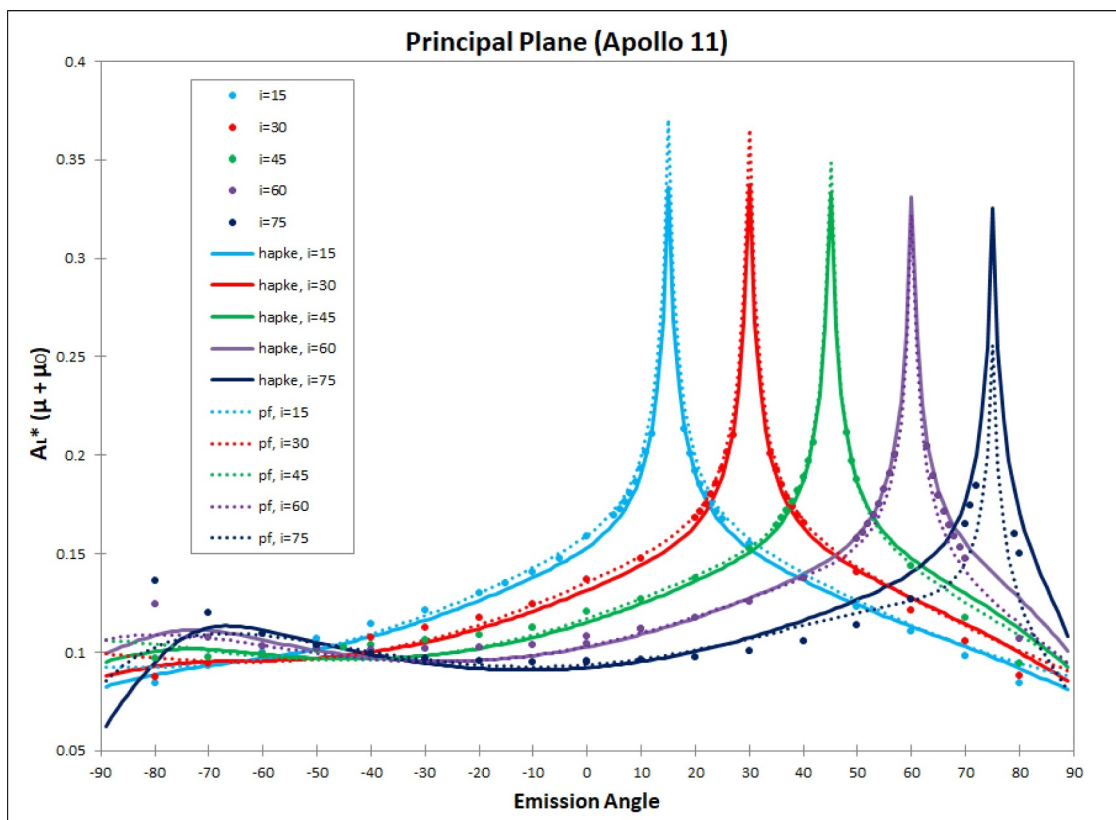


Fig. 10. Lommel Seeliger-corrected albedo plots along the principal plane. The BUG data are represented as dots, the Hapke functions are shown as solid lines and the Simplified functions are displayed as dashed lines. Both functions were calculated using the best fit parameter values shown in Table 2 for the 750 nm wavelength datasets. Each color represents a different fixed incidence angle. Both functions fit the BUG data very well at low incidence angles and do fairly well at higher incidence angles.

hemispherically integrated bolometric surface infrared emissivity, σ is the Stefan Boltzmann Constant, and T is the surface temperature. Following the work of Bandfield et al. (2015), we calculate surface temperatures using a hemispherically integrated bolometric emissivity of $\epsilon = 0.951$. To calculate bolometric brightness temperatures for normal viewing geometry to compare with the Diviner measurements described in the previous section, we use an emissivity at $e = 0^\circ$ of 0.99 as recommended by Bandfield et al. (2015).

Because we use prescribed values for $A_h(i)$ based on our simplified fits to our laboratory reflectance measurements Eqs. (8) and (9), the only remaining free parameter in the model is the H-parameter, which is the characteristic depth scale in centimeters over which the density of the lunar regolith transitions from a density of 1100 kg m^{-3} at the surface to 1800 kg m^{-3} at depth (Hayne et al., 2017). The H-parameter provides a means of gradually varying the thermal conductivity of the uppermost regolith layers. During the day, the lunar surface is close to being in radiative equilibrium, and the H-parameter does not strongly influence calculated surface temperatures. However, during the night when insolation is zero, the H-parameter strongly influences surface temperatures, with higher H-parameter values resulting in lower nighttime surface temperature (Hayne et al., 2017). Our fitting procedure involved varying the H-parameter to fit the Diviner nighttime bolometric brightness temperatures, but no effort was made to fit the Diviner daytime data.

Plots of our model-calculated normal bolometric brightness temperatures of the Apollo 11 and 16 sites using our simplified albedo parameterization are shown in Figs. 14 and 15. Also shown for comparison are normal bolometric brightness temperatures calculated using the Vasavada et al. (1999, 2012) maria and highlands albedo

parameterizations. We found that using an H-Parameter of 0.04 m provided a best fit to the nighttime data in all cases. The average difference between our model-calculated normal bolometric brightness temperatures and the Diviner data for the Apollo 11 lunar soil is $+0.11 \text{ K}$. The average difference for Apollo 16 lunar soil is -2.56 K . The average differences in the Diviner data and Vasavada's calculated temperatures for the Apollo sites are, -4.65 K for the Apollo 11 lunar soil and -8.67 K for the Apollo 16 lunar soil. The Vasavada albedos do not fit the data as well, but they were derived from a large sampling of equatorial maria and highland regions and are not optimized to provide an exact fit at the Apollo 11 and 16 sampling sites. Furthermore, Vasavada et al. (2012) fit Diviner Channel 7 brightness temperatures whereas we fit Diviner Bolometric brightness temperatures. Bandfield et al. (2015) showed that lunar surface roughness results in significantly elevated brightness temperatures at shorter wavelengths in the morning and afternoon. This causes Diviner bolometric temperatures to be higher than Channel 7 brightness temperatures in the morning and afternoon and thus explains why we require lower albedos than Vasavada et al. (2012) to accurately fit them.

8. Discussion

In total, the measurements and models we present here paint a self-consistent end-to-end picture of the solar-spectrum averaged reflectance properties of the Apollo 11 soil. Our well-calibrated bidirectional reflectance measurements of the Apollo 11 soil samples yielded solar-spectrum averaged hemispheric reflectances that produced thermal model-derived daytime bolometric brightness temperatures that are in good agreement with those measured by the well-calibrated Diviner

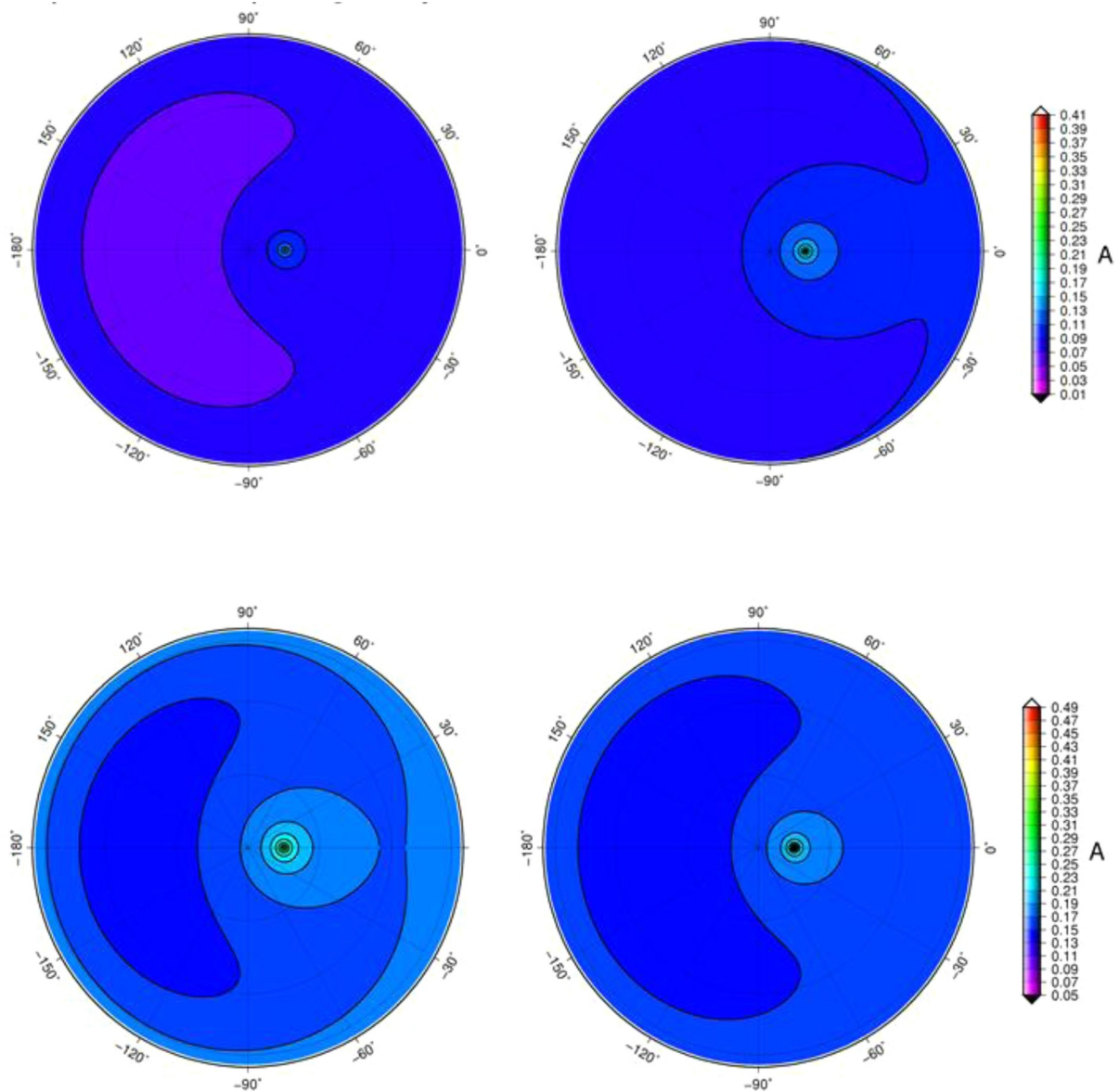


Fig. 11. Polar contour plots of modeled Lambert Albedo (A) at $i = 15$, of the Hapke (left plots) and Simplified (right plots) functions using the best fit parameter values shown in Table 2 for the 750 nm wavelength datasets. Emission is the radial coordinate and ψ is the azimuthal coordinate. The scales used here are the same as shown above for the BUG data. The top two plots were made by fitting models to the Apollo 11 data and the bottom two plots represent the Apollo 16 data.

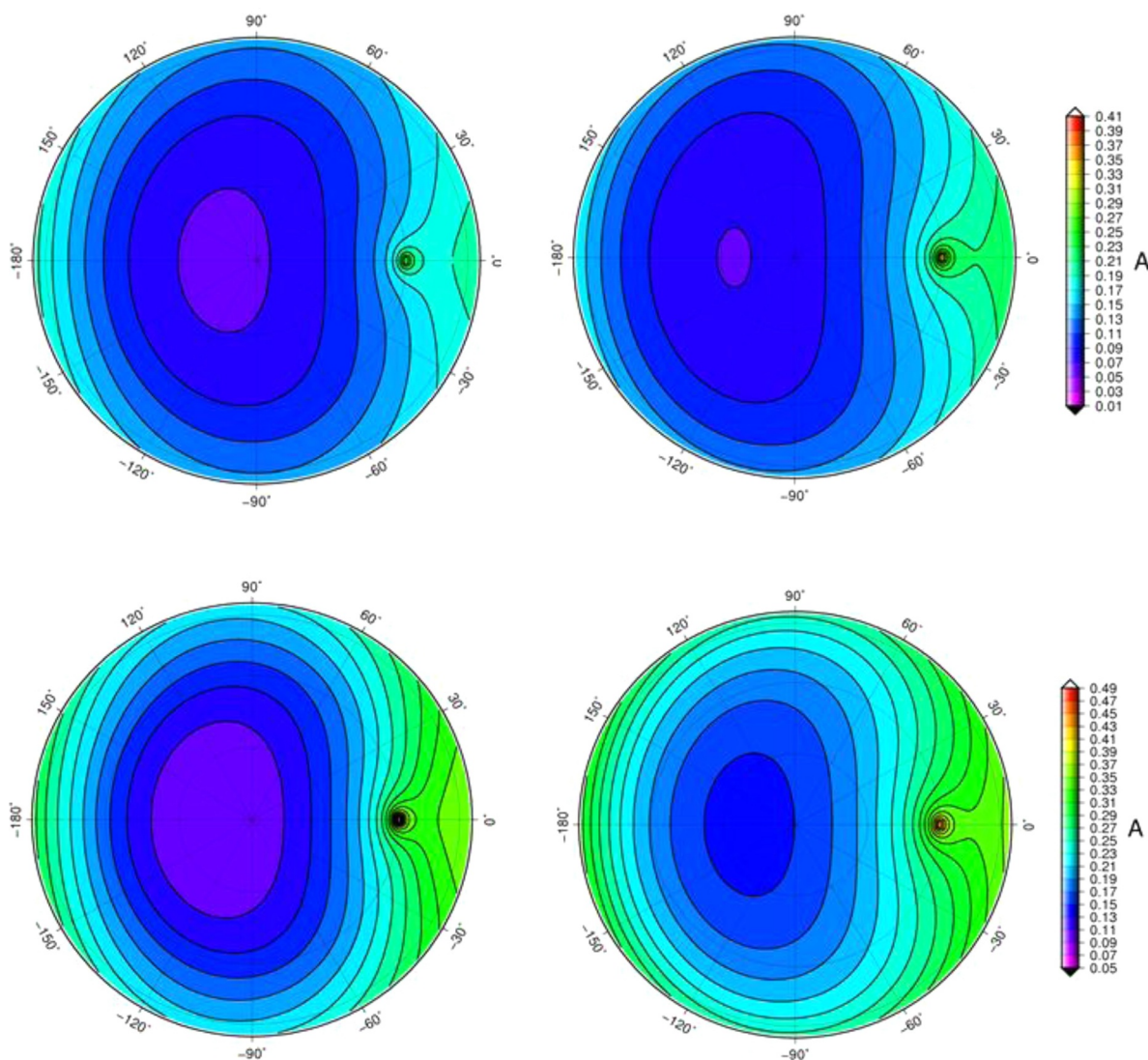


Fig. 12. BRDF polar contour plots, at $i = 60^\circ$, of Apollo 11 (top plots) and Apollo 16 (bottom plots) of the Hapke and Simplified functions using the best fit parameter values shown in Table 2 for the 750 nm wavelength datasets. The colors represent Lambert albedo, e is the radial coordinate and ψ is the azimuthal coordinate.

Table 3

Solar spectrum integration parameters employed for the calculation of A_h . Stars indicate wavelength ranges for linearly extrapolated directional hemispheric albedos.

Filter (nm)	Minimum Value (nm)	Maximum Value (nm)	Weighting Factor
200*	0	250	0.00152768008
300*	250	350	0.0379378349
450	350	500	0.174775004
550	500	650	0.196715966
750	650	850	0.186839342
950	850	1100	0.144279152
1250*	1100	1400	0.101405241
1600*	1400	1800	0.0735787377
2000*	1800	2250	0.037638206
2500*	2250	1,000,000	0.0453027375

Table 4

Derived Hapke solar-spectrum averaged parameters.

Dataset	w	b	c	θ	b0	h	χ^2_v
Apollo 11 (10,084)	0.3241379	0.3	0.3948276	8.545454	2.5	0.009375	0.273947031
Apollo 16 (61,141)	0.587931	0.3083333	0.4362069	14	2.5	0.006458333	0.1045813

instrument. This suggests that differences in the compaction states or the surface textures of our laboratory samples versus those on the natural lunar surface were not a significant factor for the case of Apollo 11. Our analysis of our goniometer BRDF measurements for Apollo 11 soil only yield a modest increase in A_h at higher incidence angles, whereas previous models have used parameterizations that imply that A_h increases very rapidly at higher incidence angles (Fig. 13). Examination of the original Birkeback et al. (1970) Apollo 11 soil integrating sphere measurements shows only a 40% increase in albedo between $i = 20^\circ$ and $i = 60^\circ$. Our goniometer results for the same sample imply 35% increase between $i = 20^\circ$ and $i = 60^\circ$, which is generally consistent. However, the Vasavada et al. (1999 and 2012) albedo parameterizations, which are based on the original model of Keihm (1984), imply a 240% increase in A_h between $i = 20^\circ$ and $i = 60^\circ$. Furthermore, the Birkeback et al. (1970) measurements only go as high as $i = 60^\circ$, so the Keihm (1984) albedo

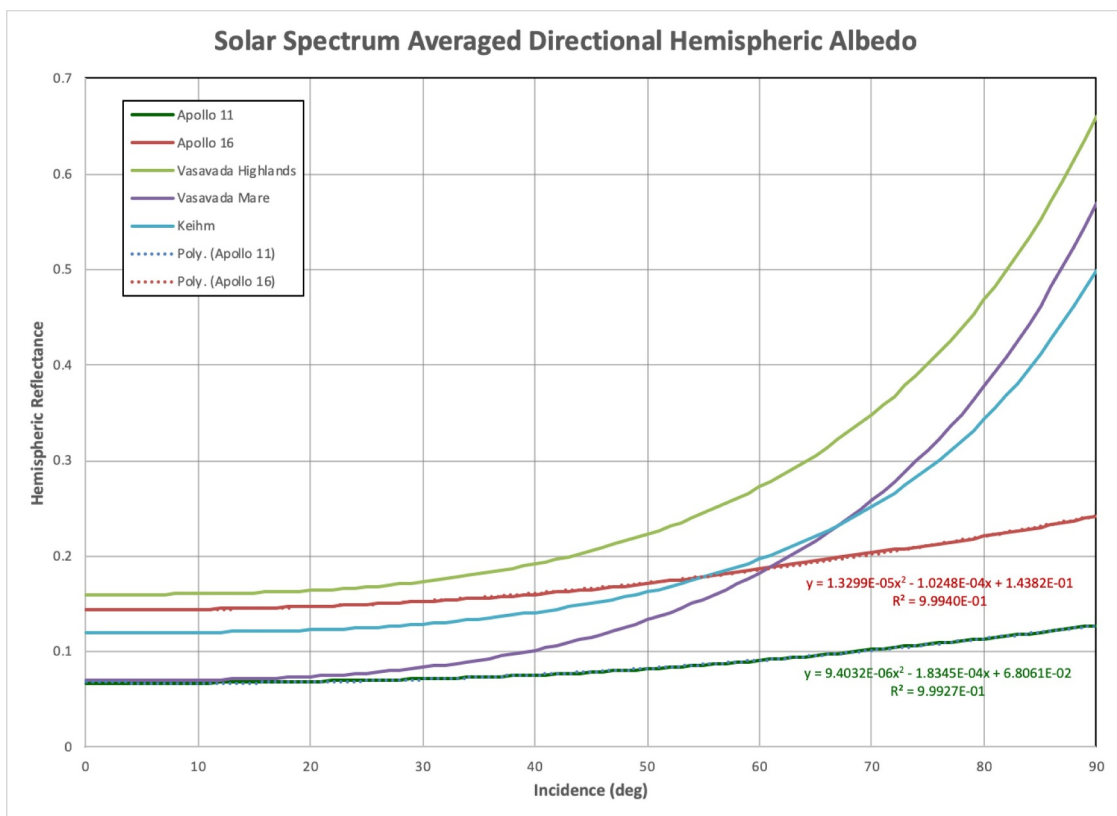


Fig. 13. Solar spectrum averaged hemispheric albedos (A_h) as a function of solar incidence angle. Shown are our best-fits based on our BUG measurements of Apollo samples, as well as the parameterizations used by Kheim (1994), and Vasavada et al. (1999, 2012). Also shown are our best fit quadratic functions for $A_h(i)$ for our Apollo 11 and Apollo 16 samples.

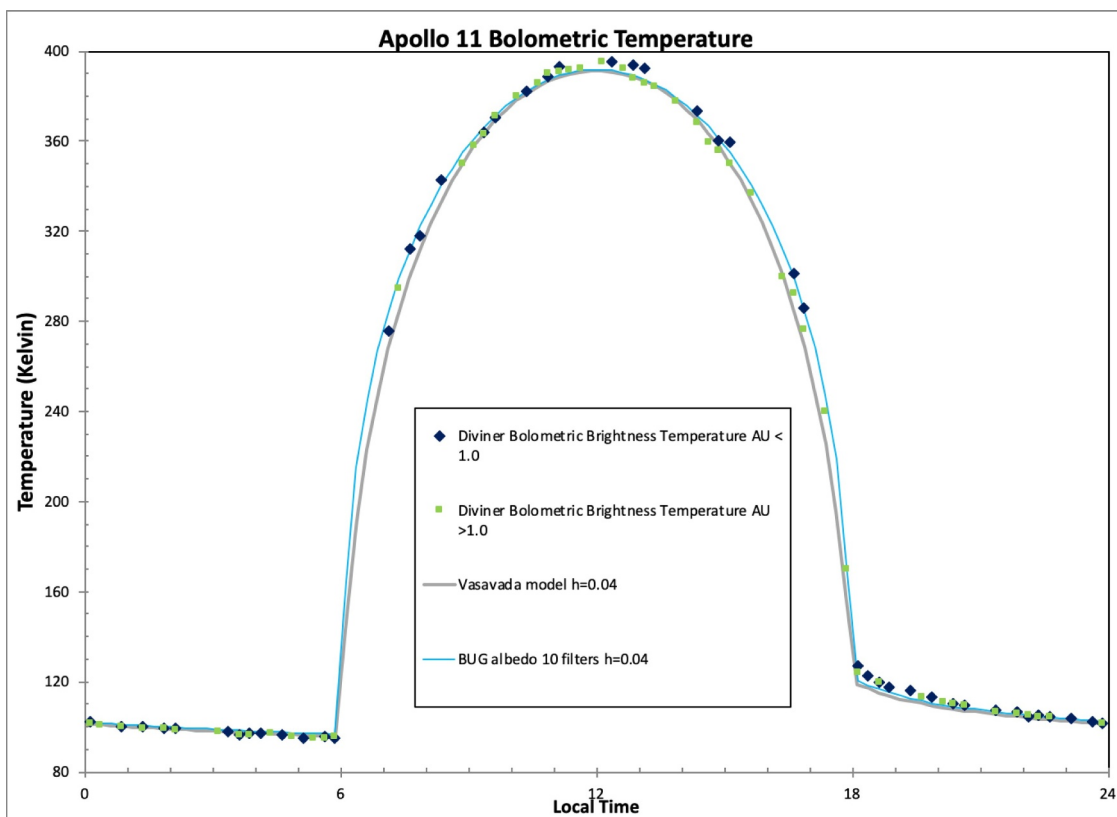


Fig. 14. Diviner measurements of normal bolometric brightness temperatures for Apollo 11 along with the results of thermal model calculations assuming our BUG albedo model functions from Fig. 13 for $A_h(i)$ those used by Vasavada et al. (2012) for equatorial lunar maria.

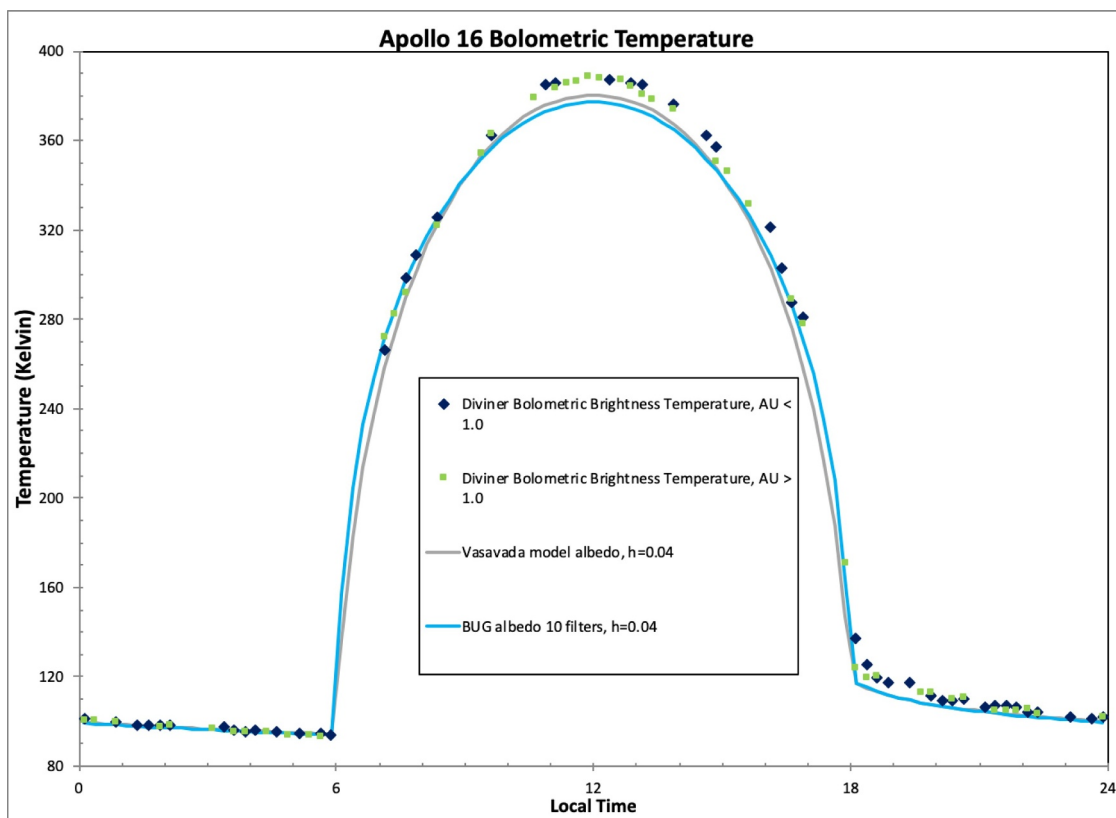


Fig. 15. Diviner measurements of normal bolometric brightness temperatures for Apollo 16 along with the results of thermal model calculations assuming our Simplified model functions from Fig. 13 for $A_h(i)$ and those used by Vasavada et al. (2012) for equatorial lunar highlands.

parameterization at higher incidence angles is an extrapolation.

The measurements and models we present here for Apollo 16 are not as self-consistent as those for Apollo 11. As shown in Fig. 14, our thermal model-calculated bolometric brightness temperatures at mid-day are distinctly lower than measured by Diviner, which implies that the Apollo 16 sample had a higher hemispheric albedo than the natural lunar surface. The solar incidence angle at the Apollo 16 site is 9.0687° at noon. Using Eq. (9), our fits to our laboratory soil reflectance measurements yield $A_h(9.0687^\circ)=0.1389$. To fit the Diviner measured T_{BolC} value of 387.5 K at noon using our thermal model would require $A_h(9.0687^\circ)=0.093$, which is approximately 33% lower than our laboratory albedo measurements would imply. Hillier et al. (1999) noted a similar discrepancy between Clementine UV/Vis Camera reflectance data and laboratory measurements of the reflectance of lunar samples. We believe that this difference could be due to some combination of two factors that have been identified in previous studies.

Ohtake et al. (2010, 2013) present comparisons between laboratory measurements of Apollo 16 sample 62,231 and SELENE Multiband Imager and Spectral Profiler (MI) measurements at the sample site, which show that the MI reflectances are 24% to 33% lower than the laboratory measurements at 750 nm. Ohtake et al. (2010) ascribe 60% of this difference to potential differences in soil composition and maturity states, and 40% to potential differences in porosity and density. As shown by Hapke (2008), increasing the filling factor (decreasing the porosity) of low to medium albedo powders increases their albedos. It is likely that the sample handling and preparation histories of our samples resulted in decreased porosities, and thus increased reflectivities. The Hapke (2008) results show that the brightening effects of decreasing porosity are greatest for medium albedo powders, which could help explain the differences in our fits between the brighter Apollo 16 soils vs the darker Apollo 11 soils. Also, given that the Apollo 16 soil samples were acquired to depths of 2–5 cm, the maturity levels of the samples are

likely lower than those of the uppermost lunar surface. We also note that the Apollo 16 field site, which included several bright recent impact craters and associated ejecta, was considerably more diverse than Apollo 11. Figs. 16 and 17 show Diviner Channel 1 Lambert Albedo maps of the 60 km lat/long boxes centered on the Apollo 11 and Apollo 16 sampling sites. The mean and standard deviations of the measured Lambert Albedos for the Apollo 11 box were 0.094 ± 0.079 , and 0.1670 ± 0.15 for the Apollo 16 box. For comparison, the measured Diviner Lambert albedos for 300 m latitude/longitude boxes centered on the Apollo 11 and Apollo 16 sample sites were 0.091 and 0.193 respectively. Although the Diviner footprint is not small enough to resolve the exact location of the Apollo 16 sample, available observations suggest that the general region sampled was 15.5% brighter than the broader field area as a whole.

9. Summary and conclusions

The principal conclusions of this study are as follows:

- 1 We obtained a complete set of calibrated BRDF measurements of 6 lunar samples acquired at two Apollo landing sites at 450, 550, 750 and 950 at incidence angles ranging from 0 to 75°
- 2 We then successfully fit the BRDF measurements to the Hapke (1993) BRDF model as well as a simplified BRDF model that we developed for this study.
- 3 We used the BRDF models to calculate the solar-spectrum averaged hemispheric reflectance as a function of solar incidence angle, which differ from those used in previous studies.
- 4 We tested the accuracy of our derived solar spectrum hemispheric reflectances by using them in a lunar thermal model to calculate normal bolometric infrared diurnal emission curves at the Apollo 11 and Apollo 16 sites.

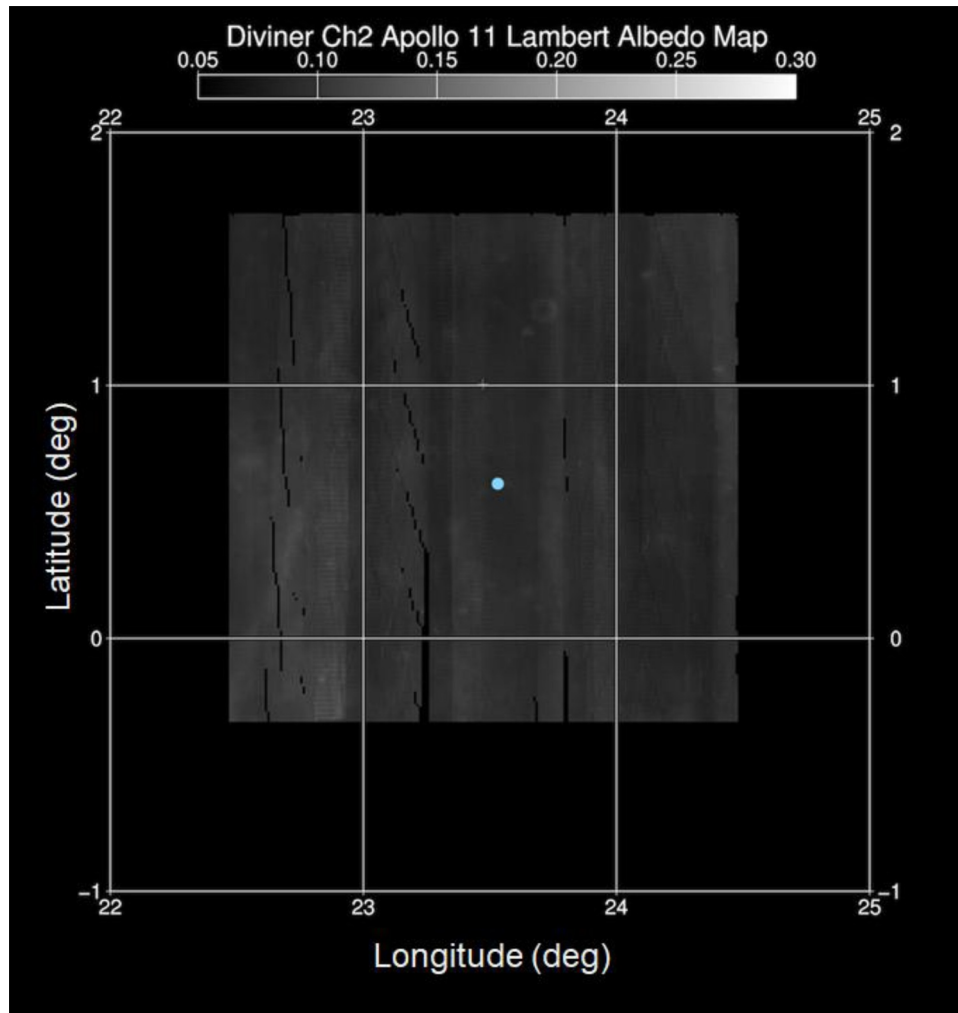


Fig. 16. Diviner Lambert Albedo Map of the Apollo 11 sample site area. The maps include Diviner Channel 2 data acquired from July 2009 - January 2017 for $0 < i < 25^\circ$ and $0 < e < 10^\circ$. The blue dot indicates the sample location for lunar soil sample 10,084. The landing site and surrounding areas appear to have homogenous reflectance properties.

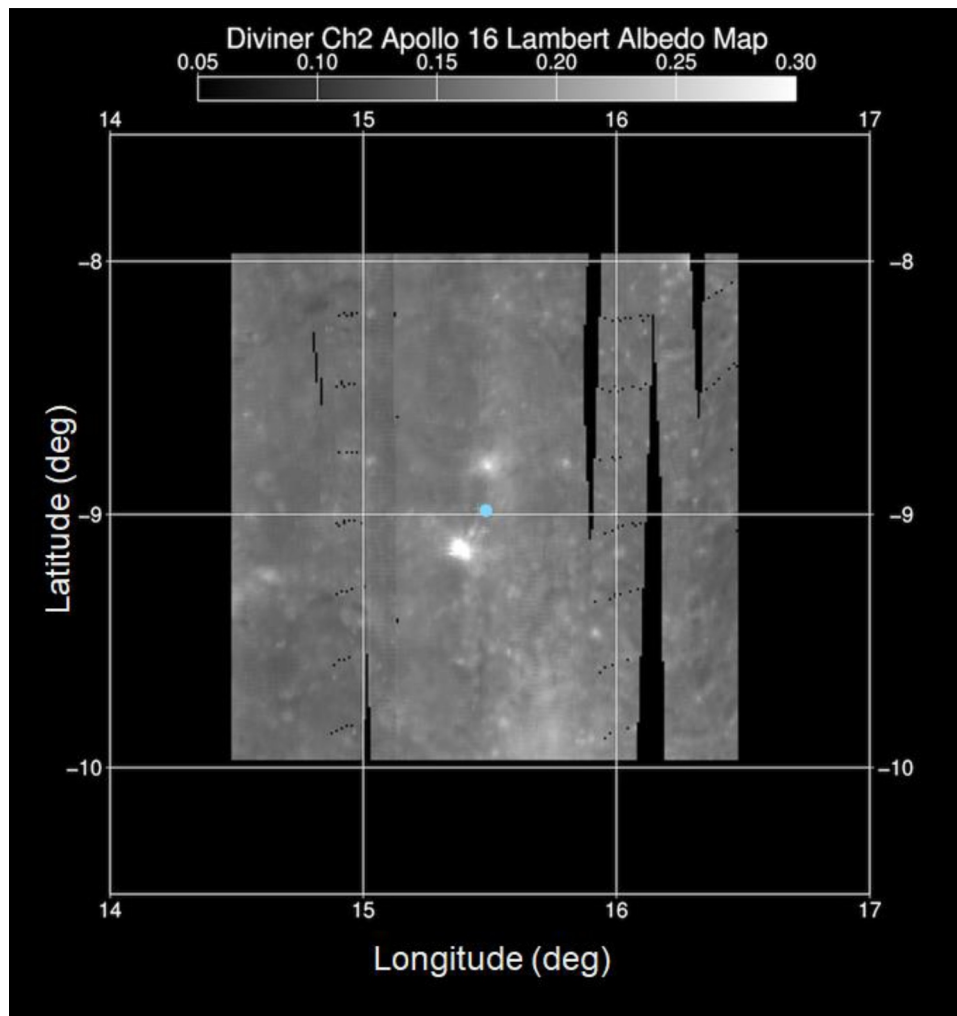


Fig. 17. Diviner Lambert Albedo Map of the Apollo 16 sample site area. The maps include Diviner Channel 2 data acquired from July 2009 - January 2017 for $0 < i < 25^\circ$ and $0 < e < 10^\circ$. The blue dot indicates the sample location for lunar soil sample 61,141 and 68,810. The Apollo 16 field site, which contained a number of fresh bright ray craters, was considerably more diverse than Apollo 11.

- 5 We compared our model-calculated normal bolometric infrared emission curves with those measured by the LRO Diviner instrument and found excellent agreement at Apollo 11, but at Apollo 16, we found that the albedos we measured in the laboratory were higher than those required to fit the Diviner infrared data
- 6 We ascribe the difference at Apollo 16 to increased compaction and decreased maturity of the laboratory sample relative to the natural lunar surface, and to local variability in surface albedos at the Apollo 16 field area that are below the spatial resolution of Diviner.

Acknowledgements

We would like to thank CAPTEM, Carl Allen and Dick Morris for generously loaning the Apollo lunar soil samples to us for this study and for their expertise on lunar soil samples. We'd also like to thank NASA Diviner LRO for funding this research. We'd also like to thank Tristram Warren and an anonymous reviewer for their detailed and insightful comments.

Supplementary materials

Supplementary material associated with this article can be found, in the online version, at [doi:10.1016/j.icarus.2019.113456](https://doi.org/10.1016/j.icarus.2019.113456).

References

- ASTM Solar Constant and Zero Air Mass Solar Spectral Irradiance Table 1 (2014) Designation: E490 – 00a.
- Bandfield, J.L., Hayne, P.O., Williams, J.P., Greenhagen, B.T., Paige, D.A., 2015. Lunar surface roughness derived from LRO Diviner Radiometer observations. *Icarus* 248, 357–372.
- Biggar, S.F., Labeled, J., Santer, R.P., Slater, P.N., Jackson, R., Moran, M.S., 1988. Laboratory calibration of field reflectance panels. *Proc. Soc. Photo-Opt. Instrum. Eng.* 924, 232–240.
- Birkebak, R.C., Cremers, C.J., Dawson, J.P., 1970. Directional spectral and total reflectance of lunar material. In: *Proceedings of the Apollo 11 Lunar Science Conference*, 3, pp. 1993–2000.
- Chandrasekhar, S., 1960. *Radiative Transfer*. Dover Publications.
- Goguen, J.D., Stone, T.C., Kieffer, H.H., Buratti, B.J., 2010. A new look at photometry of the Moon. *Icarus* 208, 548–557.
- HANDBOOK OF LUNAR SOILS, 1983 (https://curator.jsc.nasa.gov/lunar/soils/soils_hb.pdf).
- Hapke, B., 1993. *Theory of Reflectance and Emittance Spectroscopy*. Cambridge University Press.
- Hapke, B., 2008. Bidirectional reflectance spectroscopy 6. effects of porosity. *Icarus* 195, 918–926.
- Hayne, P.O., Bandfield, J.L., Siegler, M.A., Vasavada, A.R., Ghent, R.R., Williams, J.-P., Paige, D.A., 2017. Global regolith thermophysical properties of the moon from the diviner lunar radiometer experiment. *J. Geophys. Res.* 122, 2371–2400.
- Hillier, J.K., Buratti, B.J., Hill, K., 1999. Multispectral photometry of the Moon and absolute calibration of the Clementine UV/Vis camera. *Icarus* 141, 205–225.
- Izawa, M.R.M., Applin, D.M., Cloutis, E.A., Cuddy, M., Mann, P., 2014. Spectroscopic Studies of Pristine Lunar Regolith Under H₂O, O₂, and CO₂ Controlled Conditions. LPSC.

- Johnson, J.R., et al., 2006. Radiative transfer modeling of dust-coated Pancam calibration target materials: Laboratory visible/near-infrared spectrogoniometry. *JGR* 111, E02S14, 2005JE002494.
- Johnson, J.R., Shepard, M.K., Grundy, W.M., Paige, D.A., Foote, E., 2013. Spectrogoniometry and modeling of martian and lunar analog samples. *Icarus* 223, 383–406.
- Keihm, S.J., 1984. Interpretation of the lunar microwave brightness temperature spectrum: 634 feasibility of orbital heat flow mapping. *Icarus* 60 (3), 568–589.
- Korotev, R.L., Gillis, J.J., 2001. A new look at the Apollo 11 regolith and KREEP. *JGR* 106, E6.
- Milliken, Ralph E., Mustard, John F., 2007. Estimating the water content of hydrated minerals using reflectance spectroscopy I. Effects of darkening agents and low-albedo materials. *Icarus*.
- Minnaert, M., 1941. Photometry of the Moon. in *Planets and Satellites*. University of Chicago Press.
- Ohtake, M., Pieters, C.M., Isaacson, P., Besse, S., Yokota, Y., Matsunaga, T., Boardman, J., Yamamoto, S., Haruyama, J., Staid, M., Mall, U., Green, R.O., 2013. One Moon, many measurements 3: spectral reflectance. *ICARUS* Volume 226, 337–364.
- Ohtake, M., Matsunaga, T., Yokota, Y., Yamamoto, S., Ogawa, Y., Morota, T., Honda, C., Haruyama, J., Kitazato, K., Takeda, H., Iwasaki, A., Nakamura, R., Hiroi, T., Kodama, S., Otake, H., 2010. Deriving the absolute reflectance of lunar surface using selene (Kaguya) multiband imager data. *Space Sci. Rev.* 154, 57–77.
- Paige, D.A., Foote, M.T., Greenhagen, B.T., Schofield, J.T., Calcutt, S., Vasavada, A.R., Preston, D.J., Taylor, F.W., Allen, C.C., Snook, K.J., Jakosky, B.M., Murray, B.C., Soderblom, L.T., Jau, B., Loring, S., Bulharowski, J., Bowles, N., Sullivan, M.T., Avis, C., De Jong, E.M., Hartford, W., McCleese, D.J., 2010. The lunar reconnaissance orbiter diviner lunar radiometer experiment. *Space Sci. Rev.* <https://doi.org/10.1007/s11214-009-9529-2>.
- Paige, D.A., Siegler, M.A., Zhang, J.A., Hayne, P.O., Foote, E.J., Bennett, K.A., Vasavada, A.R., Greenhagen, B.T., Schofield, J.T., McCleese, D.J., Foote, M.C., De Jong, E.M., Bills, B.G., Hartford, W., Murray, B.C., Allen, C.C., Snook, K.J., Soderblom, L.A., Calcutt, S., Taylor, F.W., Bowles, N.E., Bandfield, J.L., Elphic, R.C., Ghent, R.R., Glotch, T.D., Wyatt, M.B., Lucey, P.G., 2010. Diviner lunar radiometer observations of cold traps in the moon's south polar region. *Science* 330, 479–482.
- Shepard, M.K., 2002. Initial results from the Bloomsburg University Goniometer Laboratory. *Solar Syst. Remote Sens.* 75.
- Shepard, M.K., Helfenstein, P., 2007. A test of the Hapke photometric model. *J. Geophys. Res.* 112, E03001. <https://doi.org/10.1029/2005JE002625>.
- Shepard, M.K., Helfenstein, P., 2011. A laboratory study of the bidirectional reflectance from particulate samples". *Icarus* 215, 526–533.
- Shepard, M.K., 2017. *Introduction to Planetary Photometry*. Cambridge University Press.
- Vasavada, A.R., Paige, D.A., Wood, S.E., 1999. Near-surface temperatures on Mercury and the Moon and the stability of polar ice deposits. *Icarus* 141 (2), 179–193.
- Vasavada, A.R., Bandfield, J.L., Greenhagen, B.T., Hayne, P.O., Siegler, M.A., Williams, J.P., Paige, D.A., 2012. Lunar equatorial surface temperatures and regolith properties from the Diviner Lunar Radiometer Experiment. *J. Geophys. Res.* 117 (E12).